Solar RRL

WILEY VCH

Solar RRL

RESEARCH ARTICLE OPEN ACCESS

Revealing the Crystallization Pathways of Mixed-Halide Low-Dimensional Perovskites: A First Step Toward Solar Cell Applications

Maria G. D. Guaita[1,2] | Rodrigo Szostak[2] | Francisco M. C. da Silva[2,3] | Zhihao Feng[4] | Lucas Scalon[1] | Verônica C. Teixeira[2] | Tim Kodalle[5] | Carolin M. Sutter-Fella[6] | Seung S. Jang[7] | Hélio C. N. Tolentino[2] | Ana F. Nogueira[1]

[1]Chemistry Institute (IQ), University of Campinas (UNICAMP), Campinas, Brazil | [2]Brazilian Synchrotron Light Laboratory (LNLS), Brazilian Center for Research in Energy and Materials (CNPEM), Campinas, Brazil | [3]Gleb Wataghin Physic Institute (IFGW), University of Campinas (UNICAMP), Campinas, Brazil | [4]School of Chemical & Biomolecular Engineering, Georgia Institute of Technology, Atlanta, Georgia, USA | [5]Materials Science Division and Advanced Light Source, Lawrence Berkeley National Laboratory, Berkeley, California, USA | [6]Molecular Foundry, Lawrence Berkeley National Laboratory, Berkeley, California, USA | [7]School of Materials Science and Engineering, Georgia Institute of Technology, Atlanta, Georgia, USA

Correspondence: Hélio C. N. Tolentino (helio.tolentino@lnls.br) | Ana F. Nogueira (anafla@unicamp.br)

Received: 5 June 2025 | **Accepted:** 6 June 2025

Funding: CNPq, Grant/Award Numbers: 142486/2020−5 141925/2020−5; NSF, Grant/Award Number: 2324190; FAPESP, Grant/Award Number: 2017/11986−5

Keywords: 2D perovskites | Br-rich perovskites | in situ GIWAXS | low-dimensional perovskites | Ruddlesden-Popper perovskites

ABSTRACT

Ruddlesden–Popper perovskites (RPPs) are promising materials for optoelectronic devices. While iodide-based RPPs are well-studied, the crystallization of mixed-halide RPPs remains less explored. Understanding the factors affecting their formation and crystallization are vital for optimizing morphology, phase purity, and orientation, which directly impact device performance. Here, we investigate the crystallization and properties of mixed-halide RPPs $(PEA)_2FA_{n-1}Pb_n(Br_{1/3}I_{2/3})_{3n+1}$ ($PEA = C_6H_5(CH_2)_2NH_3^+$ and $FA = CH(NH_2)_2^+$) (n = 1, 5, 10) using DMSO ($(CH_3)_2SO$) or NMP ($OC_4H_6NCH_3$) as cosolvents and MACl ($MA = CH_3NH_3^+$) as an additive. For the first time, the presence of planar defects in RPPs is directly observed by in situ grazing-incidence wide-angle X-ray scattering (GIWAXS) and confirmed through the simulation of the patterns that matched the experimental. GIWAXS data also reveals that DMSO promotes higher crystallinity and vertical orientation, while MACl enhances crystal quality but increases halide segregation, shown here by nano X-ray fluorescence (nano-XRF) experiments. For low-n RPPs, orientation is crucial for solar cell efficiency, but its impact decreases with increasing n. Our findings provide insights into optimizing mixed-halide RPPs, guiding strategies to improve crystallization, phase control, and orientation for better performance not only in solar cells but also in other potential optoelectronic devices.

1 | Introduction

Due to an additional improvement of their environmental stability compared to traditional 3D perovskites [1–3], low-dimensional Ruddlesden–Popper perovskites (RPPs) have emerged as a new family of compounds with tunable optoelectronic properties, which enable their application in optoelectronic devices, such as solar cells [4], X-ray scintillators [5], and light-emitting diodes (LEDs) [6]. Starting from the 3D structure of lead halide perovskite $APbX_3$, where A is typically Cs^+, $CH_3NH_3^+$ (methylammonium, MA) or $CH(NH_2)_2^+$ (formamidinium, FA) and X is Cl^-, Br^- or I^-, the lead halide RPP structure is formed by the addition of a bulky spacer cation (A') that does not fit into the cuboctahedron cavity of the 3D structure and causes its

cleavage, leading to the confinement of n layers of PbX_6 corner-sharing octahedra separated by A' bilayer [2, 4, 7]. These low-dimensional lead RPPs assume the chemical formula $A'_2A_{n-1}Pb_nX_{3n+1}$, where n is the number of PbX_6 octahedron layers separated by the A' bilayer. Lead halide RPPs applied in optoelectronic devices typically use aromatic group or long-chain alkyl primary amines as spacer cation A', with $C_6H_5(CH_2)_2NH_3^+$ (phenethylammonium, PEA) and $CH_3(CH_2)_4NH_3^+$ (butylammonium, BA) cations being the most studied [8–11].

The number of PbX_6 layers (n) confined on both sides by the spacer cation A' defines the dimensionality of the RPP, which is called a 2D perovskite when $n = 1$ and a quasi-2D perovskite when $n > 1$. Furthermore, the layer of large cations A' acts as a hydrophobic barrier protecting the perovskite structure from the external environment, mainly inhibiting the penetration of H_2O and O_2 into the structure and its consequent degradation [12, 13]. As a result of the decrease in dimensionality, RPPs exhibit quantum confinement, which allows the effective modulation of their optoelectronic properties, such as bandgap and exciton binding energy, by manipulating the value of n [3, 8, 14, 15]. Similar to 3D perovskite, although less explored, the ratio between the halide ions in RPPs also leads to a change in the optoelectronic properties of the material, with the increased electronegativity of the halide leading to an increase in the bandgap of the RPP for the same value of n [16–19].

Nevertheless, the preparation of low-dimensional halide RPPs entails some challenges, which include manipulating crystal orientation and controlling the distribution of phases with different values of n. The orientation of the RPP is crucial for the proper transport of charge carriers to the layers of the optoelectronic device, with the vertical orientation (the layers stacked parallel to the substrate) being the desired one [7, 11, 20]. Furthermore, due to the small difference in formation energy of phases with different n values, obtaining pure halide RPPs is quite challenging, and films produced from a solution prepared with a target n value (identified here as n') typically contain an average of n phases rather than a single pure phase [20, 21]. Thus, in general, a quasi-2D perovskite film is a multidimensional mixture containing phases with high (quasi-3D), and low values of n (quasi-2D), and $n = 1$ (2D), which leads to a distribution of bandgap energies within the film [7, 11, 21–23].

The heterogeneity in the distribution and the lack of orientation of these n-phases lead to an increase in structural defects, increasing the density of charge traps and impairing the device performance. As the extent of distribution and orientation of n-phases depend on the fabrication methods, many efforts are being directed toward understanding the influence of synthesis parameters on the final quality of the quasi-2D perovskite film. Different strategies have been employed to obtain pure and oriented quasi-2D perovskite phases, such as compositional, additive, and solvent engineering, as well as different deposition methods [7, 21].

Solvent engineering has proven to critically affect the quality of quasi-2D perovskite films because solvents have different polarities, boiling points, and coordination abilities, which drastically influence the formation mechanism. The use of a solvent mixture based mainly on dimethylformamide (DMF) is a common choice for the preparation of RPP thin films with high quality. The improvement of orientation by the addition of dimethyl sulfoxide (DMSO) as a cosolvent (the term cosolvent here is used to designate a solvent used in a smaller quantity in relation to the main solvent) is attributed to the strong interaction of DMSO molecules with Pb^{2+} which leads to the formation of intermediates that slow down the process of crystallization and enable the formation of films with much higher optical quality [7, 12, 20]. However, the interaction of the cosolvent with Pb may not be the only factor impacting the formation mechanism. For example, it is known that NMP leads to the formation of higher quality FA-based perovskites compared to DMSO, despite NMP having a lower coordination ability of Pb species than DMSO. The improved quality of FA-based perovskites with N-methylpyrrolidone (NMP) results from the formation of strong hydrogen bonds between NMP and the FA^+ cation [24–26]. This illustrates that the interaction of the solvent with all the components in the precursor solution is also a key factor in the formation mechanism and consequent film quality [25].

Additive engineering has also been used to improve the quality of RPP films. Inspired by the success achieved in 3D perovskites, MACl has been investigated as an additive for some quasi-2D perovskites, strongly impacting the n-phase distribution and orientation [7, 12, 20]. Lai et al. reported that the use of MACl on 2-thiophenemethylammonium-based perovskite with $n = 3$ resulted in a high degree of vertical orientation and an increase in power conversion efficiency (PCE) of the solar cell from 1.74 to 15.42% [27]. Recently, Lehner et al. investigated the action mechanism of MACl in MA-based RPPs through visual monitoring of the crystallization of the precursor solution in a vial during heating. However, this preparation method differs from the one used for obtaining the films used in other characterizations and solar cell assembly [28]. To date, no in situ investigations of the impact of adding MACl in the formation of crystalline structures during RPP film growth by the spin-coating method has been reported.

However, most studies investigate the effect of cosolvent and MACl additive on quasi-2D perovskites composed of MA, as the small A cation, and iodide, as X anion [7, 13, 21, 29]. In contrast, FA-based RPPs are less studied although they are considered more stable under severe operational and environmental conditions than their MA-based analogs. This difference can be partially attributed to the difficulty in obtaining high-quality FA-based RPPs in contrast to MA-based systems [30, 31]. Furthermore, although some recent reports show that the halide mixing in RPPs delivers additional control over their optoelectronic properties [18] and permits their synthesis with a wider diversity of A' spacer cations compared to single-halide RPPs [32], mixed-halide RPPs have been poorly addressed in the literature, and to our knowledge, no study on the crystallization mechanism and the factors that impact it has been performed for these materials [9]. Therefore, systematically understand the effects of composition, and the preparation method is key to develop optimized mixed-halide RPP thin films.

Here, we investigated the impact of cosolvent (DMSO and NMP), MACl addition, and variation of the target n value (n') on the formation mechanism and properties of the quasi-2D Br-rich

perovskite $(PEA)_2FA_{n-1}Pb_n(Br_{1/3}I_{2/3})_{3n+1}$ to achieve a better understanding of the effect of these variables on film quality and, ultimately, on solar cell efficiency. We studied the complete crystallization in situ during the spin-coating and thermal annealing steps using simultaneous grazing-incidence wide-angle X-ray scattering (GIWAXS) and photoluminescence spectroscopy (PL) characterizations. We observed that the impact of the additive and cosolvent on the mechanism of crystallite formation and orientation strongly depends on the n value. The films prepared with DMSO presented higher crystallinity and delivered more vertically oriented RPP. Although the films with MACl additive exhibited higher halide segregation as verified by nano X-ray fluorescence (nano-XRF), this additive was essential to produce films with higher crystallinity, orientation, and lower defect density. These parameters are correlated with high-efficiency mixed-halide RPP solar cells. Also, our data indicated that, for low-n RPPs, the major factor for obtaining efficient quasi-2D perovskites solar cells is the orientation, but the influence of this factor decreased with increasing value of n. The results reported herein allow a greater understanding of the formation dynamics and facilitate the obtaining of low-dimensional RPPs, guiding strategies to improve crystallization, phase control, and orientation of mixed RPP thin films.

2 | Results and Discussion

2.1 | Cosolvent and MACl Influence on the Formation Mechanism

To gain a deeper understanding of the impact of cosolvent type (DMSO vs. NMP) and the presence of 40 mol% of MACl additive (without MACl vs. with MACl) on the formation mechanism of RPPs, we selected $(PEA)_2FA_{n'-1}Pb_{n'}(Br_{1/3}I_{2/3})_{3n'+1}$ (n' = 1, 5, and 10) composition based on FA due to the superior environmental stability of FA-based quasi-2D perovskites compared to their MA-based counterparts [30, 31]. A mixed-halide composition was chosen as it enables greater control over material properties [18] and remains less extensively studied. The cosolvents DMSO and NMP were selected due to their distinct coordination abilities with lead species and their widespread use in the fabrication of RPP thin films [33]. The MACl concentration was determined based on a recent study demonstrating the enhanced properties of FA-based quasi-2D perovskites with 40 mol% MACl [31], which also represents the optimal concentration for improving the crystallinity of 3D perovskites [34]. The n' values of 5 and 10 were chosen because RPPs with n between 3 and 10 exhibit bandgaps suitable for solar cell applications [7]. Additionally, to achieve a more fundamental understanding of the low-dimensional system, we also investigated the 2D perovskite (n' = 1). The formation mechanism was examined through in situ multimodal characterization of all thin films, utilizing simultaneous GIWAXS and PL measurements during the preparation stages. The films prepared for in situ characterizations followed the same methodology used in the laboratory for RPP thin-film fabrication. This method consisted of a spin-coating step employing the N_2 gas-quenching method, where an N_2 jet was applied 10 s after the onset of rotation to accelerate solvent evaporation, followed by a thermal annealing step at 100°C for 4 min for the experiments performed at the synchrotron facility. The spin-coating and thermal annealing steps were carried out sequentially, avoiding any unwanted side reactions due to sample transfer. Considering the number of samples evaluated in this study (four different conditions for each of the three n' values), the analysis of the in situ results was performed in two steps. Firstly, we evaluated the influence of the cosolvent and the MACl additive on the formation mechanism for each n' value. Subsequently, we correlated the in situ data considering the n' variation.

2.1.1 | RPPs with n' = 1

Figure 1 presents the in situ GIWAXS maps as a function of time (t) and 2D patterns at specific times of the formation process for samples with n' = 1 prepared with NMP or DMSO as cosolvent and without or with MACl as additive. The in situ GIWAXS maps were obtained from the azimuthal integration of 2D patterns, resulting in 1D diffraction patterns plotted as an intensity map as a function of time (t) and scattering vector (q). Crystalline phases appear only after the N_2 jet starts, and in all n' = 1 samples, the first peak to emerge at $q \approx 7.3\ nm^{-1}$ corresponds to the (004) peak of the n = 1 $(PEA)_2Pb(Br_xI_{1-x})_4$ phase, indicating that its formation is independent of the type of the cosolvent or the presence of MACl (Figure 1a,b,g,h).

Regardless of the cosolvent, when MACl additive is used (Figure 1g,h), we observed the formation of n > 1 phases immediately after the start of the thermal annealing step, indicating the incorporation of the additive into the final structure since the added MACl is the only source of A cation required for the formation of n > 1 phases. Although the thermodynamic product is the n = 1 phase, as shown by theoretical calculations previously performed [35–37], the difference in stability is not so pronounced between the phases with n = 1, 2, or 3, leading to the formation of n > 1 phases by additive incorporation.

The position of the (004) peak of n = 1 phase (Figure S1a,b) decreases to smaller values of q (lattice expansions) with increasing temperature after the beginning of thermal annealing as expected, but during this heating stage, the peak shows a slight shift to higher q values, indicating a decrease of the lattice parameter. This behavior can be attributed to a better accommodation of the organic layer and/or the volatilization of the solvent molecules trapped in the structure or even the incorporation of I^- ions into the structure. When I^- ions are replaced by Br^- (or Cl^-) in 2D perovskite, an expansion of the unit cell occurs (in the order of 1 Å for Br^- replacing I^-) owing to the decrease in PEA-$Pb(Br,Cl)_6$ interaction by increasing the Pb-(Br,Cl) interaction compared to Pb-I [18, 38, 39]. Nevertheless, this trend does not occur for all A' cations, for example, it has been shown that BA-based RPPs presents a reduction in the distance between the layers of octahedra when I^- is replaced by Br^- [9]. Furthermore, a nonlinear variation in the distance between the layers as a function of halide substitution has been reported in the literature for the n = 2 phase based on BA^+ and MA^+ [9]. Therefore, the correlation of peak position variation with halide change strongly depends on the composition of the low-dimensional perovskite. The perovskite of interest in this study does not yet present any report with experimental or theoretical data on the influence of the halide on the distance between the layers of octahedra for phases with n > 1. Here, we indexed the peaks by considering

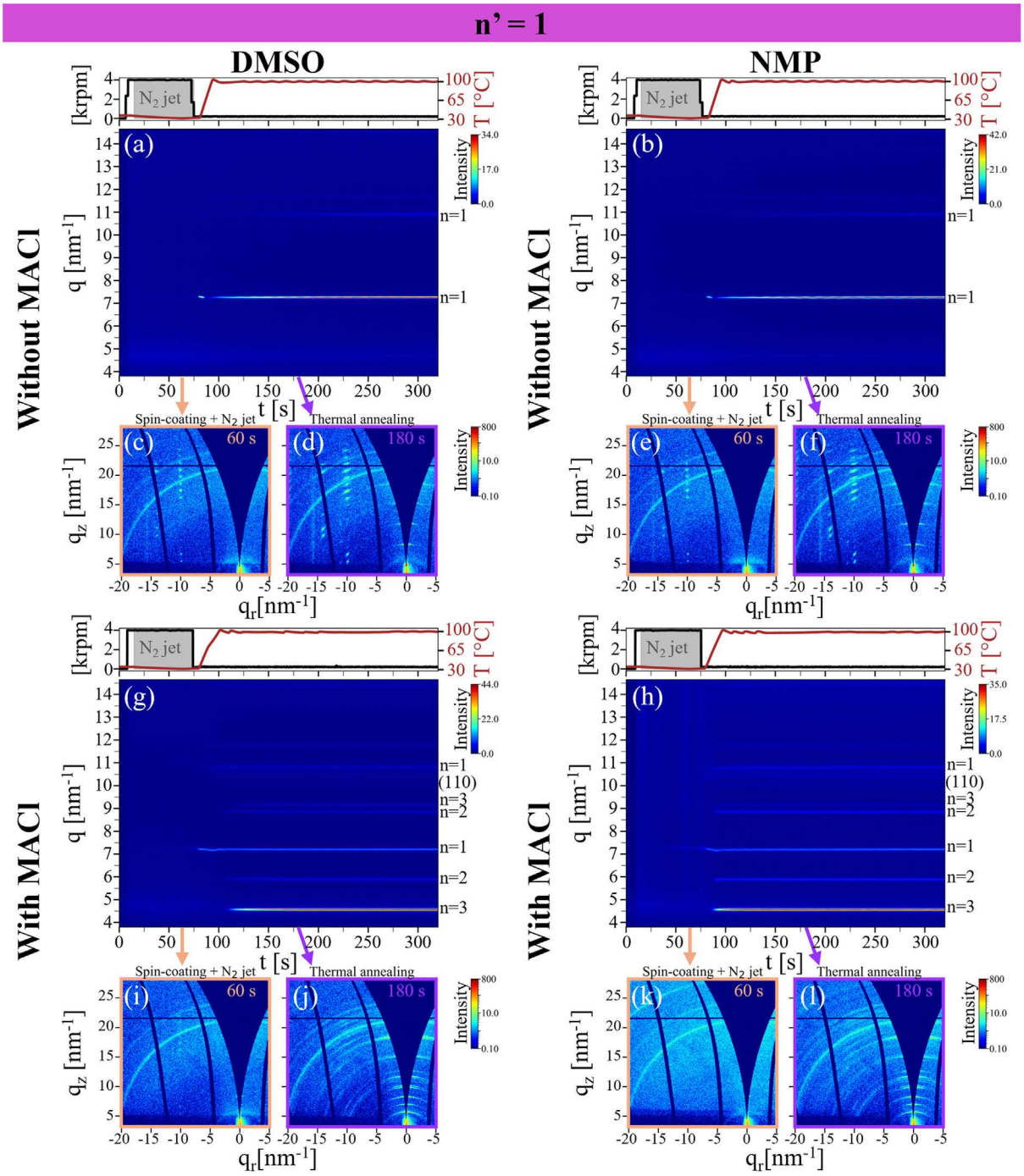

FIGURE 1 | Effect of varying the cosolvent and adding MACl on the formation of n' = 1 $(PEA)_2Pb(Br_{1/3}I_{2/3})_4$ 2D perovskite thin films during spin-coating and thermal annealing steps. (a,b,g,h) In situ GIWAXS intensity maps. 2D images of the in situ GIWAXS during: (c,e,i,k) spin-coating after the N_2 jet start ($t = 60$ s), and (d,f,j,l) thermal annealing ($t = 180$ s).

the positions closest to the peak positions of I-based 2D and quasi-2D structures reported in the literature [18, 40, 41], as Br-based quasi-2D perovskite structures are very scarce, and the system is very complex. Hence, our attribution of peak displacement as a consequence of halide substitution is done in a limited way. Moreover, the n = 1 peak position shifts to lower q when MACl is present (Figure S1a,d), indicating a higher lattice parameter, which may result from a higher incorporation of Br^- (or Cl^-) in the structure. The intensity of the 2D perovskite phase (Figure S1e,f) increases rapidly after the beginning of thermal annealing. However, when the additive is used, this increase in intensity is smaller due to competition between the n > 1 phases together with the n = 1 phase. The FWHM of the (004) peak of n = 1 (Figure S1c,d) when MACl is used is higher, showing a lower crystallinity of the phase, that is, a higher disorder of the structure, resulting from the crystallization competition between the multiples n-phases.

To verify the impact of the cosolvent and the additive on the orientation of the crystalline phases, the 2D GIWAXS patterns are

presented in Figure 1c–f, i–l. The diffraction patterns that form a complete Debye–Scherrer ring in Figure 1c–f, i–l come from the ITO used as substrate. For n' = 1, there is practically no difference in the formation mechanism and orientation when changing the cosolvent, considering the same condition of absence or presence of MACl (Figure 1). The vertical lines formed by scattering points observed in the 2D GIWAXS patterns at $q_r \approx -10$ nm^{-1} in the samples without MACl (Figure 1c–f) are characteristic of a horizontal ordering of the octahedra layers [23, 42], showing that both DMF and NMP promote a parallel orientation of the layers with the substrate. Before the thermal annealing in the samples without MACl, comparing Figure 1c with d and e with f, the horizontal stacking of the PbX_6 layers seems to be more ordered than after the thermal annealing, visualized by the distortion of the vertical points at $q_r \approx -10$ nm^{-1} and by the semi-arc formed in the position of the horizontal trace at $q_z \approx 7.2$ nm^{-1} (Videos S1, S2). This disorder may have been caused by the rapid formation of the 2D perovskite phase promoted by accelerated solvent evaporation at elevated temperatures, which causes a more disordered growth of the structure.

When MACl is used, during the spin-coating process (Figure 1i,k), the formation of the n = 1 phase with horizontal orientation is partially inhibited for both cosolvents since the intensity of the vertical points in the samples with MACl is lower than in the samples without MACl (Figure 1c compared to i and e compared to k). After the starting of the thermal annealing (Videos S3, S4), the points observed in the samples with MACl become more diffuse than in the samples without the additive, indicating a higher degree of disorder due to the formation of n > 1 phases (Figure 1i compared to j and k compared to l). It is worth mentioning that the formation of low-dimensional perovskites with vertical orientation does not generate a scattering pattern easily observable by GIWAXS. The (00l) planes (considering that the stacking direction of the structure is contained in the c-axis of the unit cell) have an in-plane orientation when the layers are perpendicular to the substrate, generating a scattering in very shallow positions ($q_z \approx 0$ nm^{-1}) and often outside the region of the reciprocal space mapped. On the other hand, in a vertical orientation, the (110) peak displays an out-of-plane orientation; however, the position of this peak is practically the same independent of the n value and coincides with the (001) peak of the 3D cubic perovskite [22, 43]. Saying that, it is not possible to determine the n value in the case of solely vertical orientation being present using only the GIWAXS data. Therefore, in samples with MACl, the appearance of the subtle (110) peak at $q \approx 10$ nm^{-1} after the start of annealing (Figure 1g,h) suggests the existence of low-n phases with vertical orientation and/or the formation of high-n phases (quasi-3D).

The in situ PL spectra of samples prepared without MACl with both cosolvents (Figure S2) show a broadening (asymmetry towards longer wavelengths) that possibly indicates intrinsic halide segregation that has occurred since the beginning of crystallization. Although this segregation is not evident in the in situ GIWAXS data, it is apparent in the X-ray diffraction (XRD) data of the final film at higher q values by the appearance of small satellite peaks (Figure S3). The literature reports an immiscibility of Br^- in I-based 2D perovskites, which results from a preferential occupation of I^- in axial positions of halide-mixed octahedra [9, 18].

The addition of MACl to achieve homogenization of the halides results in the formation of phases with n > 1, which causes the PL spectra to become broader due to the different bandgaps of the phases with different n values (Figure S2). Even though the peaks referring to the n = 2 and n = 3 phases only appear after the start of thermal annealing in GIWAXS data (Figure 1g,h), the PL data confirm that these phases have already been present since the beginning of crystallization. Therefore, these n > 1 phases initially arise during spin-coating step, without having long-range ordering to generate a diffraction pattern and crystallize during the thermal annealing step. This suggests the initial and after the thermal annealing incorporation of MACl additive in the film with n' = 1. In the thermal annealing step, the PL emission intensity decreases dramatically for all samples because of a thermal emission suppression related to increased phonon-assisted non-radiative recombination at higher temperatures [44]. The PL intensity variation in the remaining weak emission during this step is due to the low-frequency rotation required to avoid beam damage in the films during the in situ measurements.

In summary, for n' = 1, when the MACl additive is not used, and regardless of the cosolvent used, the 2D phase is formed from the beginning of crystallization with a horizontal orientation (octahedra layers parallel to the substrate) with a certain degree of halide segregation. In the samples with MACl for both cosolvents, the additive is incorporated in the structure triggering the formation of n > 1 phases with a higher orientation disorder. Therefore, no strong impact of changing the cosolvent was observed on the formation and orientation mechanism for n' = 1 films. This result is similar to that observed by Quintero-Bermúdez et al [43] where the change from DMSO to NMP did not change the horizontal orientation of the perovskite $(PEA)_2PbI_4$ prepared by the antisolvent method, showing that the same occurs when Br is added in the RPP.

2.1.2 | RPPs with n' = 5

The in situ GIWAXS for the n' = 5 quasi-2D perovskite are shown in Figure 2. For all samples, before blowing the N_2 jet, only a broad scattering at low q values ($q \approx 5$ nm^{-1}) is formed, originating from the sol–gel colloidal suspension [45, 46]. This scattering is more visible for the n' = 5 sample with NMP and without MACl (Figure 2b) because the maximum scattering intensity of this sample is lower, which causes the intensity scale of the map to be reduced, making typically weak scatterings more evident. In the two samples without MACl (Figure 2a,b), before the start of the thermal annealing ($25\ s < t < 80$ s), the formation of only the high-n phase (quasi-3D) is observed, denoted as 'α' in Figure 2, whose peak at $q \approx 10$ nm^{-1} can be indexed as (001) of the cubic perovskite phase or as (110) of the high-n RPP, because both peaks are expected at this q value [22]. After the start of thermal annealing ($t > 80$ s), weak low-n phase peaks appear in both samples without the additive. Furthermore, due to the presence of the cation FA^+ in the solution, with the acceleration of the crystallization process owing to thermal annealing, the formation of the photoinactive yellow phase δ-$FAPbI_3$ occurs, verified by the appearance of the peak at $q \approx 8.1$ nm^{-1}, denoted with 'δ' in Figure 2, in both samples without MACl.

In both samples with n' = 5 prepared with MACl (Figure 2g,h), we observed, at the same time that the α peak appeared, the

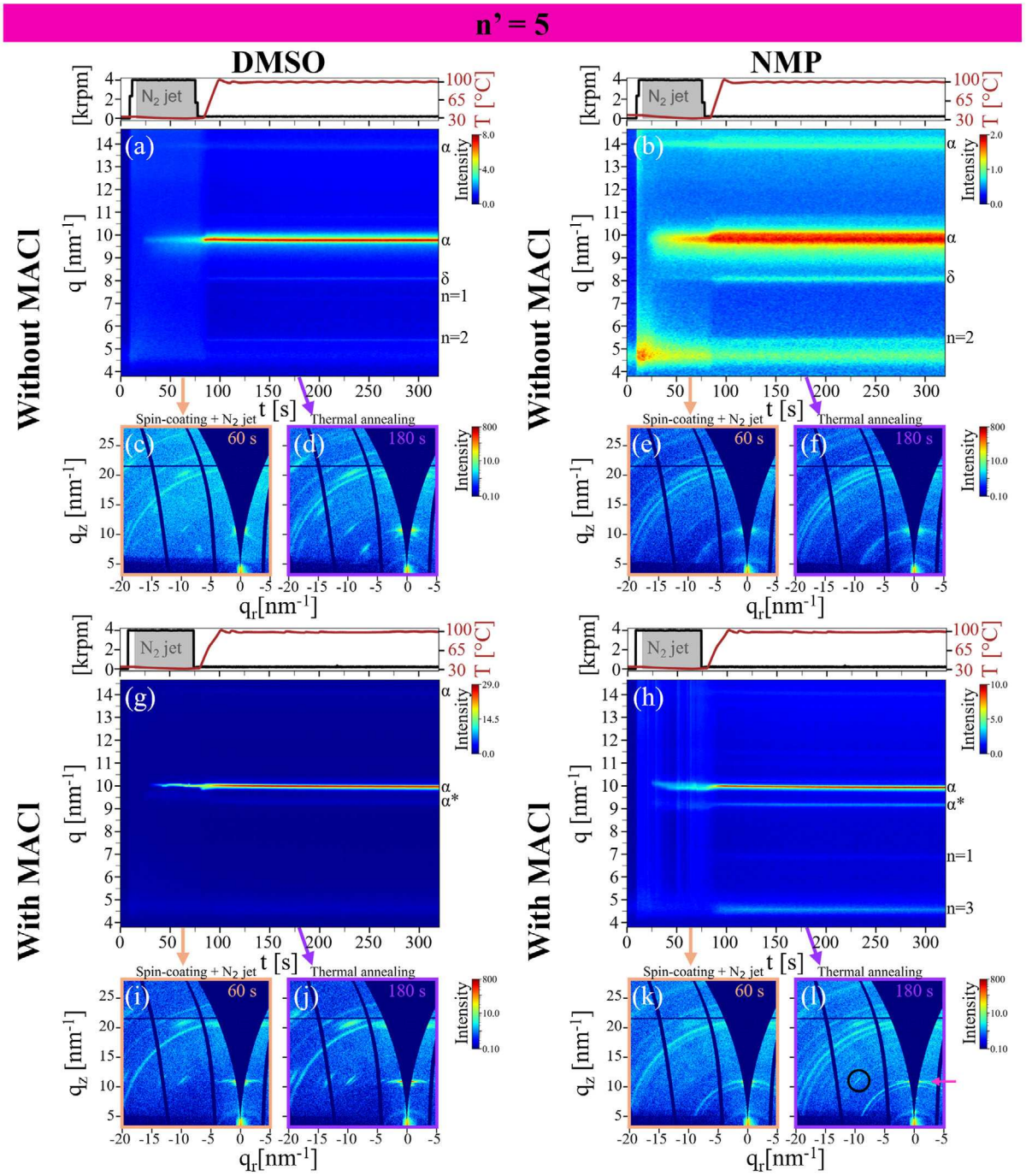

FIGURE 2 | Effect of varying the cosolvent and adding MACl on the formation of n' = 5 $(PEA)_2FA_4Pb_5(Br_{1/3}I_{2/3})_{16}$ quasi-2D perovskite thin films during spin-coating and thermal annealing steps. (a,b,g,h) In situ GIWAXS intensity maps. 2D images of the in situ GIWAXS during: (c,e,i,k) spin-coating after the N_2 jet start ($t = 60$ s) and (d,f,j,l) thermal annealing ($t = 180$ s). The symbols α and δ are used to identify the peaks referring to the yellow and high-n phases, respectively.

formation of a weaker peak at a lower q value ($q \approx 9.2$ nm^{-1}), identified in Figure 2 as 'α*'. The appearance of this peak indicates the formation of a quasi-3D phase with a higher lattice parameter, evidencing more halide segregation since the beginning of crystallization in the presence of MACl. Although the addition of MACl causes stronger halide segregation, the incorporation of the additive inhibits the formation of the photoinactive yellow phases during the thermal annealing step, which is present when the additive is not used. The inhibition of the formation of the yellow phases in the presence of MACl is observed in the literature for other compositions with FA [47].

The position of the α peak in the samples without MACl (Figure S4a, b) before the thermal annealing ($t < 85$s) is at lower q values than after the annealing ($t > 85$s), indicating a decrease in the lattice parameter with temperature, which can be attributed to the incorporation of Br^- during this step. The opposite is observed for samples with MACl, because of the evaporation of

Cl^- incorporated in the structure and the entry of Br^- or/and I^-, causing an increase in the lattice parameter. It is also verified that the position of the α peak is at higher q values in the samples with MACl, indicating the incorporation of more Br^- (or/and Cl^-) in the structure. However, this higher incorporation of Br^- (or/and Cl^-) leads to phase segregation with specific lattice parameters when MACl is present, as mentioned above. On the other hand, the crystallinity of this phase in the films prepared with MACl is higher than the films without the additive as observed by smaller FWHM values (Figure S4c,d) and higher intensity (Figure S4e,f) of the α peak.

Analyzing the 2D patterns of the in situ GIWAXS shown in Figure 2c–f, i–l, we observed a more pronounced effect of the cosolvent on the orientation for n' = 5. In the samples without MACl (Figure 2c–f), the highest orientation of the crystals is achieved when DMSO is used as a cosolvent. In the presence of NMP, the complete formation of the Debye-Scherrer rings is observed, evidencing the random orientation of the crystals.

However, when MACl is used, the orientation of the samples prepared with both cosolvents is altered. In the sample with NMP and MACl (Figure 2k,l), the formation of a more oriented phase compared to the sample with the same cosolvent but without the additive (Figure 2e,f) is observed. This improvement in orientation is evident by the presence of a higher concentration of intensity of the α peak ($q_z \approx 10$ nm^{-1}) close to $q_r \approx 0$ nm^{-1} and by the weak dot scattering at $q_z \approx 10$ nm^{-1} and $q_r \approx 10$ nm^{-1} (highlighted by the black circle in Figure 2l). This weak scattering point and a thin horizontal line at $q_z \approx 10$ nm^{-1} (highlighted in Figure 2l with a pink arrow) appear after the start of thermal annealing (Video S8) and indicate the formation of a high-n phase with an orientation parallel to the substrate in the sample with n' = 5 prepared with NMP and MACl. This same scattering line but with higher intensity and appearing since the beginning of N_2 blowing is observed for the sample prepared with DMSO and MACl (Figure 2i,j and Video S8), showing the better orientation promoted by this cosolvent in synergy with the additive.

The PL spectra of samples prepared with MACl (Figure S5c,d) are broader than the emission spectra of samples without the additive (Figure S5a,b). This broadening corroborates with what was observed in the in situ GIWAXS data regarding the segregation of phases with different amounts of halide, causing phases with different bandgaps to be present in samples with MACl, broadening the emission peak.

To summarize, for n' = 5, the influence of the cosolvent is more evident in the orientation, with DMSO promoting the formation of more oriented perovskites. It is reported in the literature that DMSO promotes higher orientation when compared to DMF alone for BA-based perovskites [14, 48, 49]. Furthermore, although the addition of the MACl additive promotes greater halide segregation, the additive inhibits the formation of the photoinactive yellow phases for both cosolvents and improves the perovskite orientation.

2.1.3 | RPPs with n' = 10

The formation of quasi-2D perovskite is strongly altered when n' is increased to 10 (Figure 3). Before the beginning of the thermal annealing ($t < 85$s), there is the formation of the high-n phase (quasi-3D) at $q \approx 10$ nm^{-1} for all conditions of n' = 10. But, for the sample with NMP and without MACl (Figure 3b), during the spin-coating step, the formation of $Pb(Br,I)_2$•NMP intermediate phase ($q \approx 5.6$ nm^{-1}) composed of $Pb(Br,I)_2$ bi-lamellae spaced by NMP solvent molecules is observed [50–52]. This intermediate is consumed as more formation of the quasi-3D phase occurs. As the temperature increases in the thermal annealing step ($t > 85$s), the intermediate quickly converts into a perovskite phase due to solvent evaporation. This intermediate phase is not observed when DMSO is used as a cosolvent (Figure 3a), probably due to the strong DMSO-Pb^{2+} interaction [33], weakening the interaction with the halide ions, which are necessary for the formation of the intermediate. For the sample prepared with DMSO and without MACl (Figure 3a), the quasi-3D perovskite crystallizes very quickly upon annealing. Such fast crystallization inhibits a homogeneous distribution of the PEA^+ cation and, as a consequence, leads to the formation of more low-n phases when compared to the sample without the additive but with NMP (Figure 3b).

When MACl is added to the sample prepared with NMP (Figure 3h), the intermediate formed in the absence of the additive is inhibited, showing the similarity between the samples with n' = 10 and n' = ∞ studied in our previous work [53]. Again, in the sample with DMSO and MACl (Figure 3g), with the beginning of thermal annealing, rapid crystallization of the quasi-3D perovskite and the following formation of low-n phases occur. Similar to what was observed for samples n' = 5, in the samples without MACl in both cosolvents (Figure 3a,b) there is the appearance of the photoinactive yellow phase (δ), which is inhibited when the additive is used (Figure 3g,h). It is also noted that in the samples with MACl, the quasi-3D phase appears in a more segregated form because of the presence of the peak identified as 'α*' in Figure 3g,h.

The position of the α peak (Figure S6a,b) is at higher q value in the samples prepared with MACl, revealing the incorporation of more Br^- (or/and Cl^-) in the structure. The crystallinity of the films prepared with MACl is higher than the films without the additive as observed by smaller values of FWHM (Figure S6c,d) and higher intensity (Figure S6e,f) of the α peak in the samples with MACl.

Similar to n' = 5, the highest orientation is obtained when DMSO is used as a cosolvent, observed by the formation of scattering points (Figure 3c,d,i,j) instead of the complete Debye–Scherrer ring in the samples with NMP (Figure 3e,f,k,l). However, in the sample with NMP and MACl (Figure 3k,l), it is observed the formation of a more oriented phase compared to the sample with the same cosolvent but without the additive (Figure 3e,f), as can be concluded due to a concentration of scattering at $q_z \approx 10$ nm^{-1}.

For the sample with DMSO and without MACl (Figure 3c,d), a cross scattering at $q_z \approx 10$ nm^{-1} is observed. This feature, highlighted in Figure 3a with a black circle, appears at the same time as the emergence of the crystalline phase (Video S9). To investigate the origin of the cross scattering, we conducted GIWAXS simulations using the reference crystallographic data of $(PEA)_2MAPb_2I_7$ [41]. As illustrated in Figures S8–S10, planar

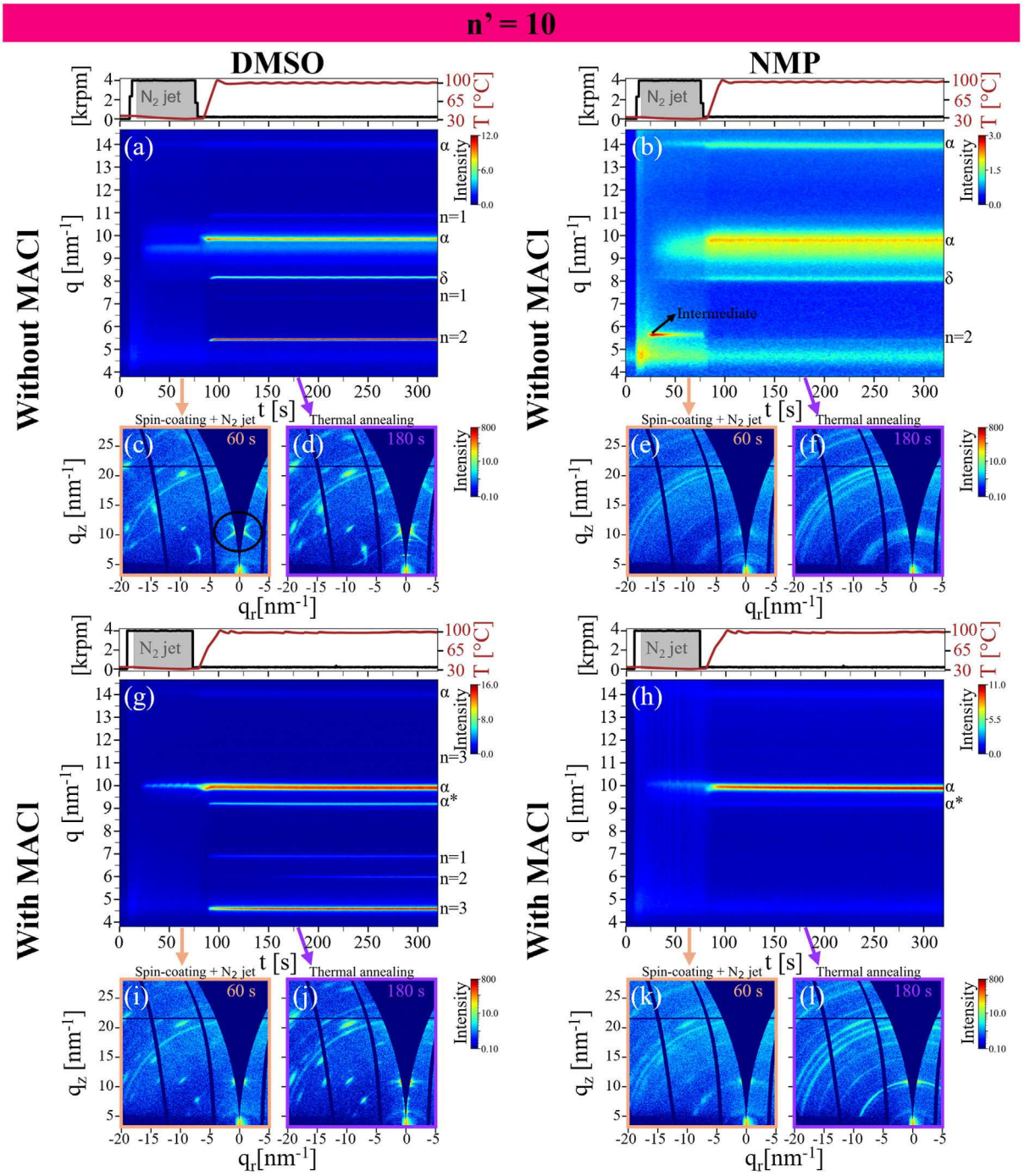

FIGURE 3 | Effect of varying the cosolvent and adding MACl on the formation of n' = 10 $(PEA)_2FA_9Pb_{10}(Br_{1/3}I_{2/3})_{31}$ quasi-2D perovskite thin films during spin-coating and thermal annealing steps. (a,b,g,h) In situ GIWAXS intensity maps. 2D images of the in situ GIWAXS during: (c,e,i,k) spin-coating after the N_2 jet start ($t = 60$ s) and (d,f,j,l) thermal annealing ($t = 180$ s). The symbols α and δ are used to identify the peaks referring to the yellow and high-n phases, respectively.

defects induced by layer translations and rotations resulted in the appearance of cross scattering at $q_z = 10$ nm^{-1}. These findings provide insight into the possible structural configurations underlying the observed cross scattering. Therefore, we attribute the cross-scattering to planar defects (stacking faults) [54–56]. Some works analyzed the presence of stacking faults in 3D perovskites by electron microscopy [57–59], other studies reported the presence of this defect in quasi-2D perovskites by examining the position shifts of the peaks in 1 diffraction [1, 60]. However, no study has reported the influence of these defects on the 2D diffraction pattern of the perovskite, such as which peaks are affected by the presence of the defect in a given plane and what distortion is caused in the scattering in the reciprocal space. Rothmann et al. were the first to observe by electron microscopy the presence of stacking faults in $FAPbI_3$ that corresponded to a shift of half a unit cell, connecting Pb-I columns with I-columns rather than Pb-I columns [58]. Li et al. showed the influence of composition and synthesis method on the types of defects and

their corresponding density, where they found that $FAPbI_3$ films had a higher density of stacking faults than $MAPbI_3$, which had a higher twinning density [57]. Pham et al. verified the influence of additives on the density of stacking faults in $FAPbI_3$ films. They found that the MACl additive increased the density of these defects in the perovskite film compared to the CsCl additive [59]. However, here we verified indirectly (through diffraction) the presence of planar defects, avoiding damage to the sample caused by the high-energy electron beam necessary for high-resolution electron microscopy. Furthermore, we observed that the addition of MACl inhibits the formation of this defect and allows a better vertical orientation of the perovskite crystals because of the absence of the cross-scattering and the presence of horizontal line scattering in the 2D diffraction pattern in Figure 3i,j.

In summary, for n' = 10, DMSO promotes the formation of more oriented perovskites, which agrees with the observed for n' = 5. In contrast, the cosolvent NMP disfavors the formation of low-n phases for n' = 10 systems, which resembles the 3D perovskite. Again, the addition of the MACl additive promotes higher halide segregation. Nevertheless, the additive inhibits the formation of the photoinactive yellow phase for both cosolvents and improves the perovskite orientation and crystallinity, reducing the defect density mainly for the DMSO sample by the disappearance of cross scattering at $q = 10\ nm^{-1}$.

2.1.4 | n' Value Influence

For n' = 1, we observed that changing the cosolvent does not change the formation mechanism or the orientation of the layers. Additionally, the additive is incorporated in the perovskite structure for both cosolvents. As the n' value increases, the influence of the additive on the orientation becomes more significant. Figure 4 outlines the effect of cosolvent and addition of MACl in RPP thin films with n' > 1. For samples with n' ≠ 1 using NMP (Figure 4b,d), we observed that the addition of MACl promotes a stronger orientation of the crystallites when compared with the samples with the same cosolvent but without the additive. However, the impact of the cosolvent is more pronounced in the orientation than the effect of the additive since the samples prepared with DMSO have a much stronger orientation even without MACl (Figure 4a). The cross scattering, attributed to the presence of planar defects, is initially present in the n' = 5 sample with DMSO and without MACl (Video S5, Supporting Information) with lower intensity than in the n' = 10 samples and is not observed when MACl is used. Then, the higher the n' value the higher the defect density when DMSO is used as cosolvent.

The stronger orientation promoted by DMSO is generally attributed to the higher interaction of DMSO with Pb^{2+}, forming intermediate complexes that delay the formation of the perovskite and lead to its slower, more ordered, and oriented growth [14, 48, 49]. Although our work shows that there is no formation of crystalline intermediates when DMSO is used, the stronger interaction of this cosolvent with Pb^{2+} [33, 61] weakens its interaction with the PEA^+ cation, leading to the formation of a monolayer of the spacer cation at the liquid-air interface, giving rise to horizontal orientation in the case of the n' = 1 system [2]. NMP molecules should interact more strongly with PEA^+ cations due to the formation of hydrogen bonds, based on the estimation with polarizability [25, 26]. However, even though the interaction with NMP-PEA^+ is stronger than that with DMSO, this interaction is insufficient to prevent the formation of the PEA^+ monolayer and avoid vertical orientation when n' = 1. When FA^+ cation is added to samples with n' > 1, the stronger DMSO-Pb^{2+} interaction, compared to NMP, favors the formation of the more crystalline and oriented quasi-3D perovskite at the liquid–air interface that serves as a support for the more oriented growth of the quasi-2D perovskite (Figure 4a,c) [2]. However, this favoring of the high-n phase crystallization with the addition of FA^+ further weakens the DMSO-PEA^+ interaction, allowing easy sliding of the layers, resulting in the presence of planar defects and the formation of low-n phases after the beginning of the thermal annealing (Figure 4a). The weaker NMP-Pb^{2+} interaction hinders the crystallization of quasi-3D perovskite phase, impeding the orientation and leading to a random distribution (Figure 4b).

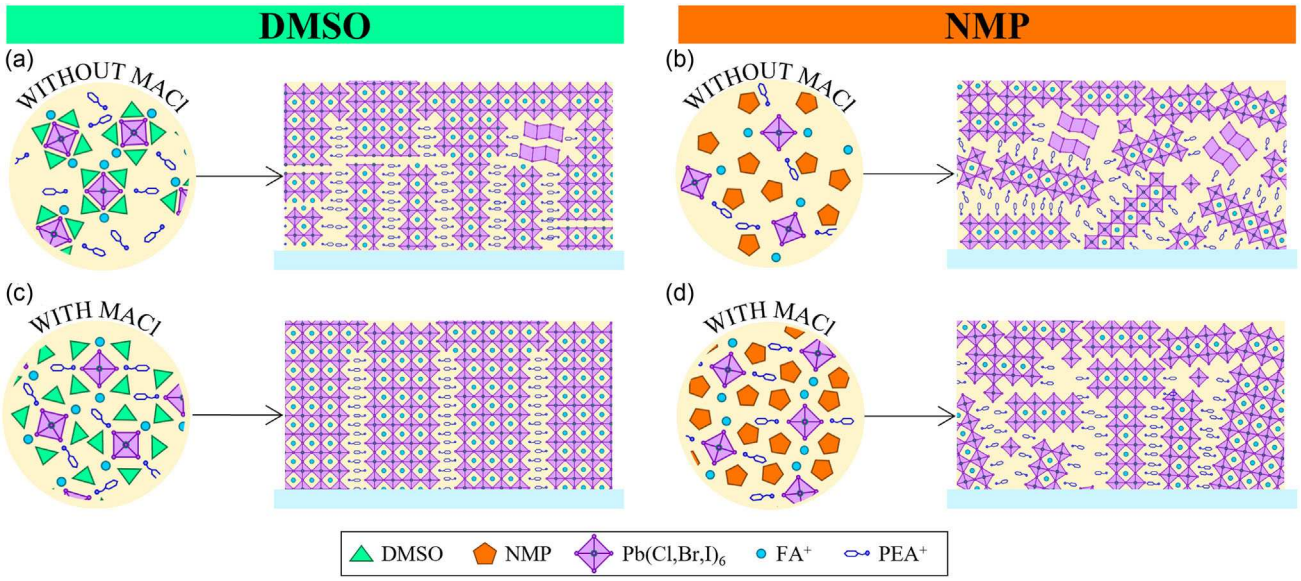

FIGURE 4 | Schematic illustration of the effect of cosolvent and addition of MACl in the orientation of $(PEA)_2FA_{n'-1}Pb_{n'}(Br_{1/3}I_{2/3})_{3n'+1}$ thin films with n' > 1. Perovskite orientation using: (a,c) DMSO, and (b,d) NMP.

With the addition of MACl, the formation of Pb-Cl bonds stronger than the Pb-I/Pb-Br bonds occurs [61], which weakens the solvent-Pb^{2+} interaction and further favors the crystallization of the quasi-3D perovskite, thus leading to the formation of more oriented films when the additive is used (Figure 4d). In addition, due to the decrease in the solvent-Pb^{2+} interaction in the presence of Cl^- anions, the DMSO-PEA^+ interaction consequently increases, which prevents the sliding of the layers, resulting in a structure with lower defect density in the presence of the additive (Figure 4c).

Although additive incorporation improves crystallinity and orientation, a higher phase segregation with MACl addition is observed. This phase segregation is more evident for lower n' values. The intensification of segregation must come from the fact that the positions in the octahedron in the RPP structure with low n value have different energies in mixed halide systems [9, 18]. Also, Lehner et al. showed that Cl^- ions are incorporated into the lattice of the I-based quasi-2D perovskite [28]. This energy difference between the positions of the octahedrons that build the RPP can become even more striking when another halide, in this case Cl^-, is added in the system. When n increases, the structure approaches the 3D system where there is no difference in energy in the positions of the octahedron so that segregation decreases.

The in situ results, summarized in Table S1 (Supporting Information), clearly show that the impact of the additive and cosolvent on the formation mechanism and crystallite orientation strongly depends on the n' value, that is, on the composition of the system. The impact of MACl on the homogenization of the halide distribution is different at the extremes of the system (2D when $n' = 1$ and 3D when $n' \to \infty$ [53]), with the additive increasing heterogeneity when n' is reduced in mixed-halide RPPs. On the other hand, crystal orientation and defect density are more strongly affected by the choice of the cosolvent, with a secondary effect of the additive reducing defect density and increasing orientation and crystallinity. Therefore, the choice of cosolvent and additive must be made considering the chosen n' value to obtain the desired properties.

2.2 | Cosolvent and MACl Influence on the Properties

Since the cosolvent and MACl impact the formation mechanism, orientation, and crystallinity, the final mixed-halide quasi-2D perovskite film properties are also expected to be different. We prepared new quasi-2D perovskite films following a method similar to the in situ experiments, however, with a complete annealing of 60 min in air. Figure 5 shows the optical absorption (OA) spectra in the UV-Vis range (dotted lines) of films with different n' values produced with and without MACl using the two different cosolvents. We observed that the samples with $n' = 1$ (Figure 5a–d) have a strong excitonic peak expected because of the quantum and dielectric confinements of the 2D perovskites [11, 12]. For samples with $n' = 1$ and MACl (Figure 5c,d), small absorption bands at wavelengths (λ) of approximately 525 and 575 nm are attributed to $n = 2$ and $n = 3$ phases, also verified by the in situ GIWAXS data. When n' increases to 5 (Figure 5e–h), the absorption of low-n phases (small bands at $\lambda < 600$ nm) is still evident; however, for samples $n' = 5$ prepared with MACl (Figure 5g,h), the absorption at $\lambda \approx 700$ nm (attributed to the quasi-3D phase) is higher than for the films without the additive (Figure 5e,f). For samples with $n' = 10$ (Figure 5i–l), the absorption attributed to the quasi-3D phase ($\lambda \approx 700$ nm) becomes higher in samples with the additive (Figure 5i,j), while the absorption of low-n phases ($\lambda < 600$ nm) becomes less evident with MACl.

Figure 5 also presents the PL spectra obtained by illuminating the samples from the film-air interface (front, in continuous line) and the substrate-air interface (back, filled curve in Figure 5). For $n' = 1$ (Figure 5a–d), the heterogeneity in the Br^- distribution throughout the film depth occurs regardless of the cosolvent or the presence of the additive, as visualized by the difference between the emission position when the film is excited from the front or from the back. The small band at $\lambda \approx 580$ nm is derived from the emission of $n > 1$ phases present in samples prepared with MACl (Figure 5c,d). For films with $n' > 1$ (Figure 5e–l), the band at $\lambda \approx 750$ nm is attributed to the emission of the quasi-3D phase. Despite the OA spectra showing the presence of low-n phases, the emission at $\lambda < 600$ nm from these phases is almost not detected on the film surface, showing the segregation of phases with different n values along the film depth, which is particularly evident for films without MACl (Figure 5e,f,i). The literature reports this segregation of the distribution of different n values phases throughout the depth of quasi-2D perovskite films, with lower-n phases more concentrated at the film bottom and higher-n phases at the surface of the film, as observed here [29, 62]. The nondetection of emission from low-n phases in samples with MACl reveals the better coupling between phases with different bandgaps resulting from the improved crystallinity with the use of the additive, causing only the emission from the phase with the smallest bandgap (quasi-3D) to be observed.

To evaluate the impact of the cosolvent and the addition of MACl on halide distribution homogeneity in the samples with different n' values, we performed nano-XRF mappings over an area of $5 \times 5\ \mu m^2$ employing a synchrotron X-ray nanoprobe (Carnaúba beamline at Sirius) [63], controlling the dose to reduce the beam damage. The ratio of Br by Pb emission, shown in Figure 6, allows accounting for morphology and thickness effects based on the assumption that Pb is homogeneously distributed in the films [64]. The increase in the size of the domains with Br deficiency (reddish areas on the maps in Figure 6) or Br excess (bluish areas) in the samples prepared with MACl (Figure 6c,d,g,h,k,l) indicates that the addition of the additive enhances (micro-)heterogeneities in the horizontal halide distribution in all samples. This result corroborates with was observed by in situ GIWAXS measurements, which showed higher halide segregation with the formation of crystalline phases with different lattice parameters when MACl is used. Other studies have reported heterogeneities in the Br distribution on quasi-2D perovskites using other techniques with lower spatial resolution than the nano-XRF used in this work [15, 39].

Our results revealed for the first time the increased heterogeneity of Br distribution in the presence of MACl in mixed-halide RPPs. This behavior can be attributed to the stronger Pb–Cl interaction [61] and to the Cl^- incorporation in the quasi-2D perovskite as observed by the Cl small peaks in the X-ray photoelectron

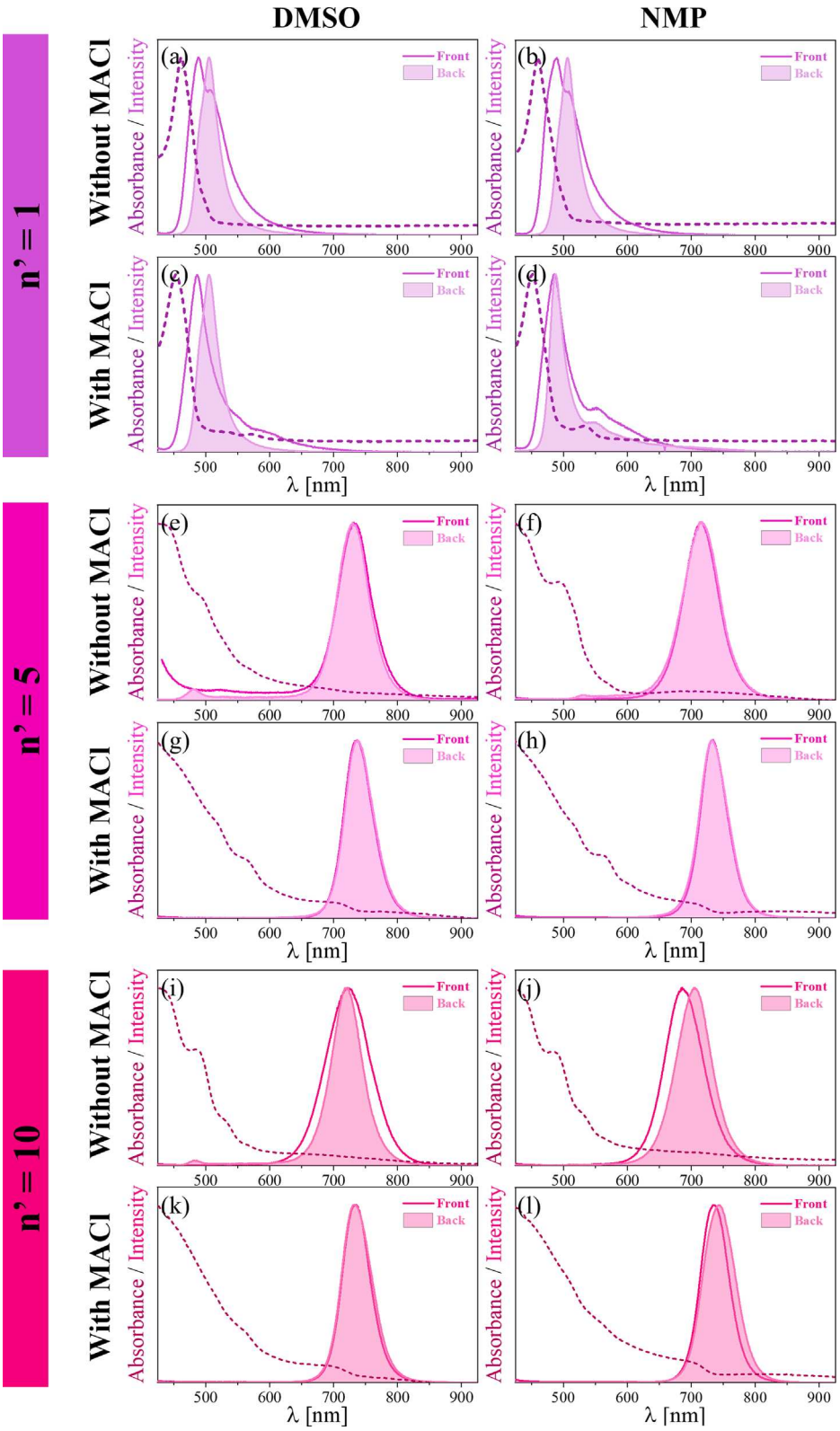

FIGURE 5 | OA (dotted lines) and PL (continuous line for surface film and filled curve for substrate side) spectra of $(PEA)_2FA_{n'-1}Pb_{n'}(Br_{1/3}I_{2/3})_{3n'+1}$ thin films prepared with (a–d) n' = 1, (e–h) n' = 5, and (i–l) n' = 10.

spectroscopy (XPS) data (Figure S12). The incorporation of MACl into quasi-2D perovskites was also observed in other works for different compositions [10, 28, 65]. Lehner et al. showed that the additive was trapped inside the films due to the crystallization of an intermediate, stabilized by Cl^-, whose crystallization begins at the air–liquid interface, forming a cap layer that acts as a barrier that prevents the complete evaporation of MACl [28]. However, our in situ GIWAXS results do not indicate the formation of crystalline intermediates in the presence of MACl but show that the quasi-3D phase is formed initially (Figure 1). Furthermore, the

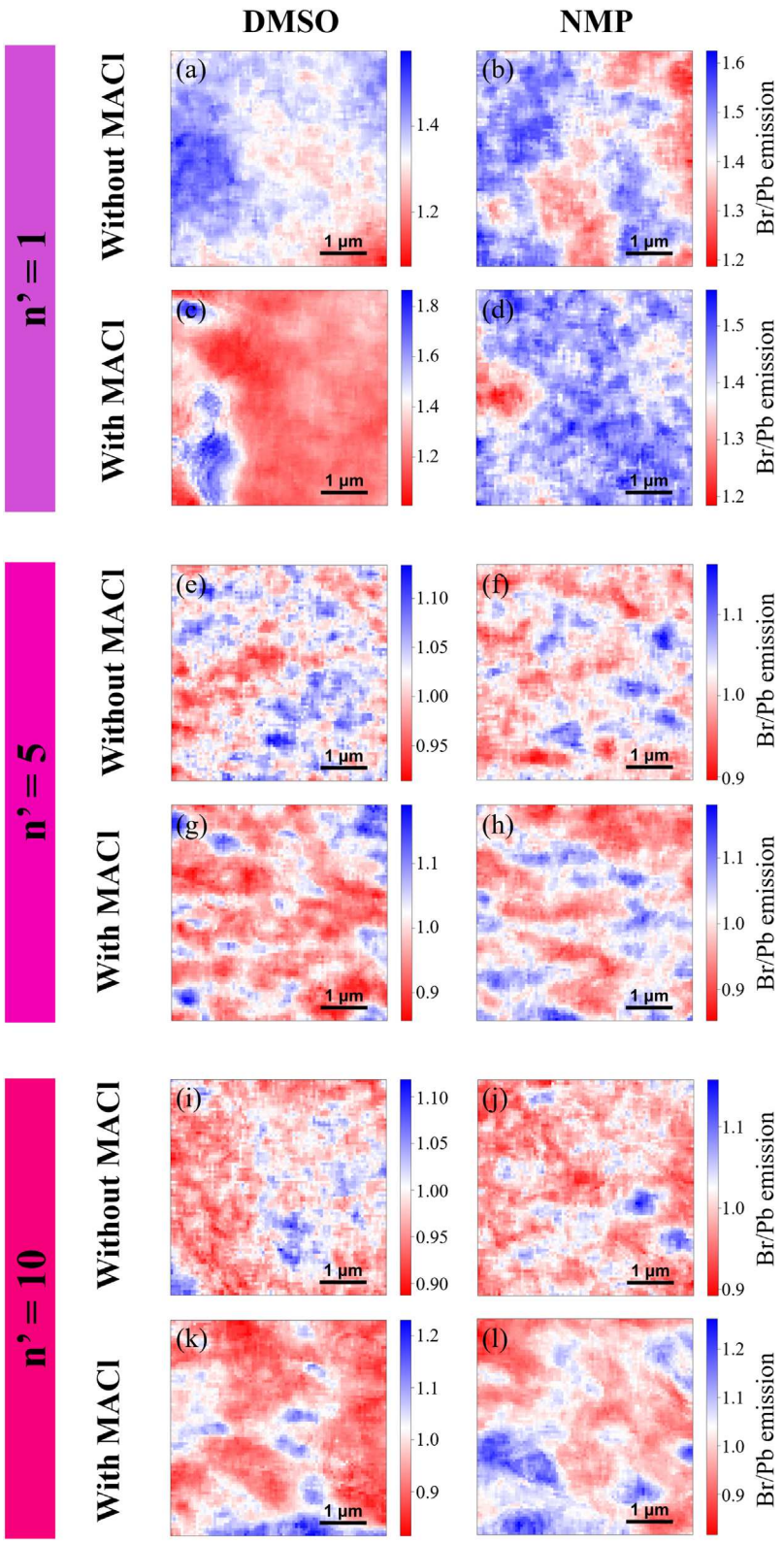

FIGURE 6 | Effect of varying the cosolvent, and n', and adding MACl on the halide distribution observed by nano-XRF of $(PEA)_2FA_{n'-1}Pb_{n'}(Br_{1/3}I_{2/3})_{3n'+1}$ thin films prepared with (a–d) n' = 1, (e–h) n' = 5, and (i–l) n' = 10.

in situ PL data of sample n' = 1 with MACl (Figure S2) show that the incorporation of MACl, and the consequent formation of n > 1 phases, occurs since the beginning of the crystallization. Still, the presence of these n > 1 phases due to MACl incorporation in n' = 1 samples is observed at the top of the film by the ex situ PL spectra in Figure 5, indicating that the incorporation of MACl does not occur due to the formation of a barrier for its evaporation. We believe that the incorporation of the MACl additive in quasi-2D perovskites is related to the formation of stronger Pb-Cl bonds [61] and higher energy stabilization

through the incorporation of Cl^- resulting from the energy difference between the positions of the octahedrons that build the RPP structure [9, 18].

2.3 | Cosolvent and MACl Influence on the Solar Cell Performance

To investigate the influence of the cosolvent, MACl additive, and n' variation on the photovoltaic performance, we prepared and characterized mixed-halide quasi-2D perovskite solar cells using the n-i-p architecture: glass/FTO/SnO_2/Perovskite/Spiro-OMeTAD/Au. Samples with n' = 1 have been previously characterized here for fundamental understanding, however, perovskite devices with n' = 1 were not prepared because they do not have bandgap suitable for application in solar cells. Therefore, only compositions with n' = 5, and 10, that have a wide bandgap (Figure 5) appropriate for tandem cells, were evaluated. The photovoltaic parameters statistics of the solar cells are shown in Figure 7 and the *J–V* curves and parameters of champion devices are shown in Figure S13 and Table S2. When NMP cosolvent is used, it is observed that the orientation and crystallinity increased by the addition of MACl (Figures 2 and 3) is essential to improve the performance of the device. However, the orientation promoted by the additive in RPPs with NMP as cosolvent is lower than that observed when DMSO is used. Thus, the PCE close to n' = 10 quasi-2D perovskites with NMP and DMSO, both with MACl (Figure 7), shows that the higher the n' value, the smaller the impact of the orientation on the efficiency of the photovoltaic device.

Interestingly, for films prepared with DMSO we observed that, although the orientation is evident regardless of the presence of the additive, a high PCE is only achieved when MACl is used (Figure 7). Therefore, we conclude that the orientation of the crystallites is more important for the performance of the quasi-2D perovskite device than the halide distribution homogeneity, but the orientation is not the only relevant parameter. Even when the orientation is adequate, but a high density of defects is present, which occurs in films prepared with DMSO without MACl due to the presence of planar defects, the device performance is strongly impacted. The highest PCEs obtained were 11.75%, 11.55%, and 9.45% for the compositions n' = 5 DMSO, n' = 10 DMSO, and n' = 10 NMP, all with MACl, respectively. Although Wei et al. have recently shown the beneficial effect of Br doping in quasi-2D perovskite solar cells [66], to our knowledge, this is the first work studying the effects of synthesis parameters on the formation mechanism, halide homogeneity, and photovoltaic device performance of Br-rich quasi-2D perovskites.

3 | Conclusion

In this work, the formation of mixed-halide low-dimensional perovskites was investigated by evaluating the influence of the cosolvent, MACl additive, and n' value variation through simultaneous in situ GIWAXS and PL measurements. Through extensive analysis, we established correlations among the formation mechanism, properties, and photovoltaic performance of mixed-halide quasi-2D perovskites. The in situ characterizations revealed that the impact of the cosolvent is dependent on the n' value, providing valuable insights into the design of precursor solutions that lead to the formation of RPPs with enhanced properties. The investigation of halide distribution heterogeneity at the submicron scale on RPPs represents a novel and significant contribution to the field. For the first time, the presence of planar defects in RPPs was directly observed by GIWAXS and confirmed through the simulation of the patterns that matched the experimental data. Furthermore, the suppression of these defects was achieved by the addition of MACl. While MACl incorporated into quasi-2D perovskites was found to induce higher halide segregation, the additive role in enhancing crystallinity, orientation, and reducing defect density was determined to be crucial for the fabrication of efficient Br-rich RPP solar cells, as demonstrated for the first time in this study. Additionally, our in-depth investigation into the formation of mixed-halide RPPs provides a clear understanding of the interactions among the components of the precursor solution, which

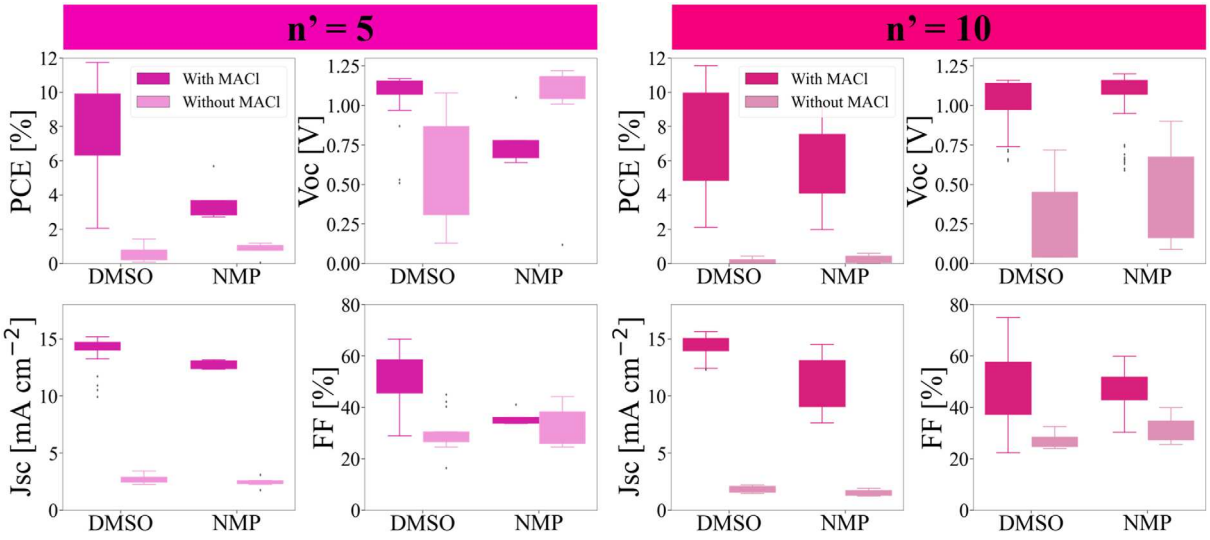

FIGURE 7 | Effect of varying the cosolvent and *n*' and adding MACl on the parameters' statistics obtained by *J–V* measurements of $(PEA)_2FA_{n'-1}Pb_{n'}(Br_{1/3}I_{2/3})_{3n'+1}$ without and with MACl solar cells.

directly influence the emergence of planar defects, compositional homogeneity, and, consequently, the final material properties. Therefore, our findings can be broadly applied to other compositions, offering strategic direction for optimizing crystallization, phase control, and orientation to achieve RPPs with superior properties.

Acknowledgements

M.G.D.G. thanks CNPq for the scholarships (grant 142486/2020−5). R.S. acknowledges FAPESP (grant 2021/01357−6). F.M.C.S. thanks CNPq for the scholarships (grant 141925/2020−5). L.S. thanks FAPESP (grant 2020/04406−5). T.K. acknowledges funding by the US Department of Energy (DOE), Office of Science, Office of Basic Energy Sciences, Materials Sciences and Engineering Division, under contract no. DE-AC02-05-CH11231 (D2S2 program KCD2S2). V.C.T. acknowledges the L'Óreal-UNESCO-ABC for the prize "For Women in Science" (Physics, Brazil, 2023). Z.F. and S.S.J. acknowledge support from NSF award no. 2324190. The authors gratefully acknowledge support from CNPq, FAPESP (grants 2017/11986−5), Shell, and the support of ANP (Brazil's National Oil, Natural Gas, and Biofuels Agency) through the R&D levy regulation. Also, the authors thank Antonio A. M. Gasperini for his support in processing the GIWAXS 2D patterns. This research used facilities of the Brazilian Synchrotron Light Laboratory (LNLS), part of the Brazilian Center for Research in Energy and Materials (CNPEM), a private nonprofit organization under the supervision of the Brazilian Ministry for Science, Technology, and Innovations (MCTI). The CARNAUBA/LNLS staff is acknowledged for their assistance during the beamtime and sample preparation. The authors particularly acknowledge the use of the in situ spin-coater available at beamline 12.3.2 of the ALS as well as supporting work from Nobumichi Tamura and Jonathan Slack. The ALS is a DOE Office of Science User Facility under contract no. DE-AC02-05CH11231. Work at the Molecular Foundry was supported by the Office of Science and Office of Basic Energy Sciences of the US Department of Energy (contract DE-AC02-05CH11231).

The Article Processing Charge for the publication of this research was funded by the Coordenação de Aperfeiçoamento de Pessoal de Nível Superior - Brasil (CAPES) (ROR identifier: 00x0ma614).

Conflicts of Interest

The authors declare no conflicts of interest.

Data Availability Statement

The data that support the findings of this study are available from the corresponding author upon reasonable request.

References

1. A. S. Tutantsev, E. I. Marchenko, N. N. Udalova, et al., "Structural Disorder in Layered Hybrid Halide Perovskites: Types of Stacking Faults, Influence on Optical Properties and Their Suppression by Crystallization Engineering," *Nanomaterials* 11 (2021): 3333.

2. A. Z. Chen, M. Shiu, J. H. Ma, et al., "Origin of Vertical Orientation in Two-Dimensional Metal Halide Perovskites and Its Effect on Photovoltaic Performance," *Nature Communications* 9 (2018): 1336.

3. A. N. Yadav, S. Min, H. Choe, J. Park, and J. Cho, "Halide Ion Mixing across Colloidal 2D Ruddlesden-Popper Perovskites: Implication of Spacer Ligand on Mixing Kinetics," *Small* 20 (2024): 2305546.

4. C. Wang, X. Dong, F. Chen, G. Liu, and H. Zheng, "Recent Progress of Two-Dimensional Ruddlesden-Popper Perovskites in Solar Cells," *Materials Chemistry Frontiers* 7 (2023): 5786–5805.

5. Y. Li, Y. Lei, H. Wang, and Z. Jin, "Two-Dimensional Metal Halides for X-Ray Detection Applications," *Nano-Micro Letters* 15 (2023): 128.

6. S. Yudco and L. Etgar, "Ruddlesden-Popper and Dion-Jacobson Perovskites in Multiple Quantum Wells Light-Emitting Diodes," *Advanced Optical Materials* 12 (2024): 2302592.

7. A. Caiazzo and R. A. J. High Janssen, "Efficiency Quasi-2D Ruddlesden-Popper Perovskite Solar Cells," *Advanced Energy Materials* 12 (2022): 2202830.

8. F. Huang, P. Siffalovic, B. Li, et al., "Controlled Crystallinity and Morphologies of 2D Ruddlesden-Popper Perovskite Films Grown without Anti-Solvent for Solar Cells," *Chemical Engineering Journal* 394 (2020): 124959.

9. S.Toso, I.Gushchina, A. G.Oliver, L.Manna, M.Kuno, "Are Mixed-Halide Ruddlesden-Popper Perovskites Really Mixed?," *ACS Energy Letters* 7 (2022): 4242–4247.

10. X. Li, W. Hu, Y. Shang, et al., "Phenylformamidinium-Enabled Quasi-2D Ruddlesden-Popper Perovskite Solar Cells with Improved Stability," *Journal of Energy Chemistry* 66 (2022): 680–688.

11. X. Zhao, T. Liu, and Y.-L. Loo, "Advancing 2D Perovskites for Efficient and Stable Solar Cells: Challenges and Opportunities," *Advanced Materials* 34 (2022): 2105849.

12. Y. Xu, M. Wang, Y. Lei, Z. Ci, and Z. Jin, "Crystallization Kinetics in 2D Perovskite Solar Cells," *Advanced Energy Materials* 10 (2020): 2002558.

13. T. L. Leung, I. Ahmad, A. A. Syed, et al., "Stability of 2D and Quasi-2D Perovskite Materials and Devices," *Communications Materials* 3 (2022): 63.

14. A. Caiazzo, K. Datta, J. Jiang, et al., "Effect of Co-Solvents on the Crystallization and Phase Distribution of Mixed-Dimensional Perovskites," *Advanced Energy Materials* 11 (2021): 2102144.

15. S. J. Yang, K. Wang, Y. Luo, et al., "Two-Factor Phase Separations in Mixed-Halide Quasi-2D Perovskite LEDs: Dimensionality and Halide Segregations," *ACS Energy Letters* 8 (2023): 3693–3701.

16. N. K. Nobuaki Kitazawa, "Compositional Modulation of Two-Dimensional Layered Perovskite (RNH3)2Pb(Cl, Br, I)4 and Its Optical Properties," *Japanese Journal of Applied Physics* 35 (1996): 6202.

17. N. Kitazawa, "Excitons in Two-Dimensional Layered Perovskite Compounds: (C6H5C2H4NH3)2Pb(Br, I)4 and (C6H5C2H4NH3) 2Pb(Cl," *Br)4. Materials Science and Engineering: B* 49 (1997): 233–238.

18. N. E. Wright, X. Qin, J. Xu, et al., "Influence of Annealing and Composition on the Crystal Structure of Mixed-Halide, Ruddlesden-Popper Perovskites," *Chemistry of Materials* 34 (2022): 3109–3122.

19. X. Qi, L. Yang, X. Wang, et al., "Vertical Halide Segregation and Stability of Two-Dimensional Layered Perovskite Nanostructures: Implications for Optoelectronic Devices," *ACS Applied Nano Materials* 6 (2023): 16309–16317.

20. P. Liu, N. Han, W. Wang, et al., "High-Quality Ruddlesden-Popper Perovskite Film Formation for High-Performance Perovskite Solar Cells," *Advanced Materials* 33 (2021): 2002582, Preprint at, https://doi.org/10.1002/adma.202002582.

21. H. Gu, J. Xia, C. Liang, et al., "Phase-Pure Two-Dimensional Layered Perovskite Thin Films," *Nature Reviews Materials* 8 (2023): 533–551.

22. W. L. Tan and C. R. McNeill, "X-Ray Diffraction of Photovoltaic Perovskites: Principles and Applications," *Applied Physics Reviews* 9 (2022): 021310.

23. J. A. Steele, E. Solano, D. Hardy, et al., "How to GIWAXS: Grazing Incidence Wide Angle X-Ray Scattering Applied to Metal Halide Perovskite Thin Films," *Advanced Energy Materials* 13 (2023): 2300760.

24. R. Szostak, S. Sanchez, P. E. Marchezi, et al., "Revealing the Perovskite Film Formation Using the Gas Quenching Method by In Situ GIWAXS: Morphology, Properties, and Device Performance," *Advanced Functional Materials* 31 (2021): 2007473.

25. Y. Han, S. Park, J. Wang, et al., "Controlling Spatial Crystallization Uniformity and Phase Orientation of Quasi-2D Perovskite-Based Light-Emitting Diodes Using Lewis Bases," *Advanced Materials Interfaces* 7 (2020): 1901860.

26. J.-W. Lee, Z. Dai, C. Lee, et al., "Tuning Molecular Interactions for Highly Reproducible and Efficient Formamidinium Perovskite Solar Cells via Adduct Approach," *Journal of the American Chemical Society* 140 (2018): 6317–6324.

27. H. Lai, B. Kan, T. Liu, et al., "Two-Dimensional Ruddlesden-Popper Perovskite with Nanorod-Like Morphology for Solar Cells with Efficiency Exceeding 15%," *Journal of the American Chemical Society* 140 (2018): 11639–11646.

28. L. E. Lehner, S. Demchyshyn, K. Frank, et al., "Elucidating the Origins of High Preferential Crystal Orientation in Quasi-2D Perovskite Solar Cells," *Advanced Materials* 35 (2023): 2208061.

29. X. Li, J. M. Hoffman, and M. G. Kanatzidis, "The 2D Halide Perovskite Rulebook: How the Spacer Influences Everything from the Structure to Optoelectronic Device Efficiency," *Chemical Reviews* 121 (2021): 2230–2291.

30. J. V. Milić, S. M. Zakeeruddin, and M. Grätzel, "Layered Hybrid Formamidinium Lead Iodide Perovskites: Challenges and Opportunities," *Accounts of Chemical Research* 54 (2021): 2729–2740.

31. M. Liu, D. Zheng, T. Zhu, et al., "2D Halide Perovskite Phase Formation Dynamics and Their Regulation by Co-Additives for Efficient Solar Cells," *Advanced Materials Interfaces* 11 (2024): 2300773.

32. J. Ovčar, T. L. Leung, L. Grisanti, et al., "Mixed Halide Ordering as a Tool for the Stabilization of Ruddlesden-Popper Structures," *Chemistry of Materials* 34 (2022): 4286–4297.

33. J. C. Hamill Jr., J. Schwartz, and Y.-L. Loo, "Influence of Solvent Coordination on Hybrid Organic-Inorganic Perovskite Formation," *ACS Energy Letters* 3 (2018): 92–97.

34. M. Kim, G. H. Kim, T. K. Lee, et al., "Methylammonium Chloride Induces Intermediate Phase Stabilization for Efficient Perovskite Solar Cells", *Joule* 3 (2019): 2179–2192.

35. L. N. Quan, M. Yuan, R. Comin, et al., "Ligand-Stabilized Reduced-Dimensionality Perovskites," *Journal of the American Chemical Society* 138 (2016): 2649–2655.

36. J. Xing, Y. Zhao, M. Askerka, et al., "Color-Stable Highly Luminescent Sky-Blue Perovskite Light-Emitting Diodes," *Nature Communications* 9 (2018): 3541.

37. T. Jiang, H. Min, R. Zou, et al., "Molecularly Controlled Quantum Well Width Distribution and Optoelectronic Properties in Quasi-2D Perovskite Light-Emitting Diodes," *Journal of Physical Chemistry Letters* 13 (2022): 4098–4103.

38. K. Du, Q. Tu, X. Zhang, et al., "Two-Dimensional Lead(II) Halide-Based Hybrid Perovskites Templated by Acene Alkylamines: Crystal Structures, Optical Properties, and Piezoelectricity", *Inorganic Chemistry* 56 (2017): 9291–9302.

39. C. R. Roy, Y. Zhou, D. D. Kohler, et al., "Intrinsic Halide Immiscibility in 2D Mixed-Halide Ruddlesden-Popper Perovskites," *ACS Energy Letters* 7 (2022): 3423–3431.

40. I. C. Smith, E. T. Hoke, D. Solis-Ibarra, M. D. McGehee, and H. I. Karunadasa, "A Layered Hybrid Perovskite Solar-Cell Absorber with Enhanced Moisture Stability," *Angewandte Chemie International Edition* 53 (2014): 11232–11235.

41. M. A. K. Sheikh, D. Kowal, M. H. Mahyuddin, et al., "A2Bn-1PbnI3n+1 (A = BA, PEA; B = MA; n = 1, 2): Engineering Quantum-Well Crystals for High Mass Density and Fast Scintillators," *The Journal of Physical Chemistry C* 127 (2023): 10737–10747.

42. R. L. Milot, R. J. Sutton, G. E. Eperon, et al., "Charge-Carrier Dynamics in 2D Hybrid Metal-Halide Perovskites," *Nano Letters* 16 (2016): 7001–7007.

43. R. Quintero-Bermudez, A. Gold-Parker, A. H. Proppe, et al., "Compositional and Orientational Control in Metal Halide Perovskites of Reduced Dimensionality," *Nature Materials* 17 (2018): 900–907.

44. M. Liu, Q. Wan, H. Wang, et al., "Suppression of Temperature Quenching in Perovskite Nanocrystals for Efficient and Thermally Stable Light-Emitting Diodes," *Nature Photonics* 15 (2021): 379–385.

45. R. Szostak, P. E. Marchezi, A. D. S. Marques, et al., "Exploring the Formation of Formamidinium-Based Hybrid Perovskites by Antisolvent Methods: In Situ GIWAXS Measurements during Spin Coating," *Sustainable Energy Fuels* 3 (2019): 2287–2297.

46. R. Munir, A. D. Sheikh, M. Abdelsamie, et al., "Hybrid Perovskite Thin-Film Photovoltaics: In Situ Diagnostics and Importance of the Precursor Solvate Phases," *Advanced Materials* 29 (2017): 1604113.

47. K. Odysseas Kosmatos, L. Theofylaktos, E. Giannakaki, et al., "Methylammonium Chloride: A Key Additive for Highly Efficient, Stable, and Up-Scalable Perovskite Solar Cells," *Energy and Environmental Materials* 2 (2019): 79–92, Preprint at, https://doi.org/10.1002/eem2.12040.

48. J. Zhang, L. Zhang, X. Li, et al., "Binary Solvent Engineering for High-Performance Two-Dimensional Perovskite Solar Cells," *ACS Sustainable Chemistry & Engineering* 7 (2019): 3487–3495.

49. L. Gao, F. Zhang, C. Xiao, et al., "Improving Charge Transport via Intermediate-Controlled Crystal Growth in 2D Perovskite Solar Cells," *Advanced Functional Materials* 29 (2019): 1901652.

50. S. Mahesh, J. M. Ball, R. D. J. Oliver, et al., "Revealing the Origin of Voltage Loss in Mixed-Halide Perovskite Solar Cells," *Energy Environmental Science* 13 (2020): 258–267.

51. F. Cheng, X. Jing, R. Chen, et al., "N-Methyl-2-Pyrrolidone as an Excellent Coordinative Additive with a Wide Operating Range for Fabricating High-Quality Perovskite Films," *Inorganic Chemistry Frontiers* 6 (2019): 2458–2463.

52. J. Cao, X. Jing, J. Yan, et al., "Identifying the Molecular Structures of Intermediates for Optimizing the Fabrication of High-Quality Perovskite Films," *Journal of the American Chemical Society* 138 (2016): 9919–9926.

53. M. G. D. Guaita, R. Szostak, F. M. C. da Silva, et al., "Influence of Methylammonium Chloride on Wide-Bandgap Halide Perovskites Films for Solar Cells", *Advanced Functional Materials*, 34 (2023): 2307104.

54. A. Boulle, D. Chaussende, L. Latu-Romain, et al., "X-Ray Diffuse Scattering from Stacking Faults in Thick 3C-SiC Single Crystals," *Applied Physics Letters* 89 (2006): 091902.

55. A. Boulle, D. Chaussende, L. Latu-Romain, et al., "Determination of Stacking Fault Densities in 3C-SiC Crystals by Diffuse X-Ray Scattering", *Physica Status Solidi A*, 204 (2007): 2528–2534.

56. A. Boulle, D. Chaussende, F. Conchon, G. Ferro, and O. Masson, "Characterization of Stacking Faults in Thick 3C-SiC Crystals Using High-Resolution Diffuse X-Ray Scattering," *Journal of Crystal Growth* 310 (2008): 982–987.

57. W. Li, M. U. Rothmann, Y. Zhu, et al., "The Critical Role of Composition-Dependent Intragrain Planar Defects in the Performance of MA1-xFAxPbI3 Perovskite Solar Cells," *Nature Energy* 6 (2021): 624–632.

58. M. U. Rothmann, J. S. Kim, J. Borchert, et al., "Atomic-Scale Microstructure of Metal Halide Perovskite (1979)," *Science* 370 (2020): eabb5940.

59. H. T. Pham, Y. Yin, G. Andersson, et al., "Unraveling the Influence of CsCl/MACl on the Formation of Nanotwins, Stacking Faults and Cubic Supercell Structure in FA-Based Perovskite Solar Cells," *Nano Energy* 87 (2021): 106226.

60. W. L. Tan, Y.-B. Cheng, and C. R. McNeill, "Direct Assessment of Structural Order and Evidence for Stacking Faults in Layered Hybrid

Perovskite Films from X-Ray Scattering Measurements," *Journal of Materials Chemistry A: Materials* 8 (2020): 12790–12798.

61. R. Schier, A. Conesa Rodriguez, A. M. Valencia, and C. Cocchi, "Formation of Lead Halide Perovskite Precursors in Solution: Insight from Electronic-Structure Theory," *Physica Status Solidi B* 258 (2021): 2100359.

62. T. Liu, Y. Jiang, M. Qin, et al., "Tailoring Vertical Phase Distribution of Quasi-Two-Dimensional Perovskite Films via Surface Modification of Hole-Transporting Layer," *Nature Communications* 10 (2019): 878.

63. H. C. N. Tolentino, R. R. Geraldes, F. M. C. da Silva, et al., "The CARNAÚBA X-Ray Nanospectroscopy Beamline at the Sirius-LNLS Synchrotron Light Source: Developments, Commissioning, and First Science at the TARUMÃ Station," *Journal of Electron Spectroscopy and Related Phenomena* 266 (2023): 147340, https://doi.org/10.1016/j.elspec.2023.147340-10.1016/j.elspec.2023.147340.

64. K. Frohna, M. Anaya, S. Macpherson, et al., "Nanoscale Chemical Heterogeneity Dominates the Optoelectronic Response of Alloyed Perovskite Solar Cells," *Nature Nanotechnology* 17 (2022): 190–196.

65. L. Deng, H. Yang, Z. Liu, et al., "Effective Phase Control for High-Performance Red-Light-Emitting Quasi-2D Perovskite Solar Cells via MACl Additive," *ACS Applied Energy Materials* 4 (2021): 2856–2863.

66. Y. Wei, Y. Sun, Y. Liu, et al., "Impact of Bromide Incorporation on Strain Modulation in 2D Ruddlesden-Popper Perovskite Solar Cells," *Cell Reports Physical Science* 4 (2023): 101739.

Supporting Information

Additional supporting information can be found online in the Supporting Information section.